

Non-planar illumination deflectometry for axicon metrology

HENRY QUACH,¹ HYUKMO KANG,¹ BYEONGJOON JEONG,¹ HEEJOO CHOI,^{1,2} AND DAEWOOK KIM^{1,2,3,*}

¹Wyant College of Optical Sciences, University of Arizona, 1630 E. University Blvd., Tucson, Arizona 85721, USA

²Large Binocular Telescope Observatory, University of Arizona, 933 N Cherry Ave., Tucson, Arizona 85721, USA

³Department of Astronomy and Steward Observatory, University of Arizona, 933 N. Cherry Ave., Tucson, Arizona 85721, USA

*Corresponding author: dkim@optics.arizona.edu

Received 26 May 2022; revised 30 June 2022; accepted 30 June 2022; posted 1 July 2022; published 19 July 2022

We introduce an on-axis deflectometry test configuration for axicon metrology. Axicons are challenging to measure due to their characteristically steep, convex geometry. However, if an axicon is coaxially aligned with a camera and a surrounding cylindrical illumination source, high-resolution surface measurements can be obtained via the principle of deflectometry. Emitted from the temporally modulated source, light deflects at the conical surface and into the entrance pupil of a camera, illuminating the full axicon aperture except the \varnothing 0.5-mm rounded tip. Deflectometry measurements of a 100° and 140° axicon show holistic cone angle agreement within 0.035° against touch probe data and up to 7.93 root μm mean square difference from a best-fit cone. We discuss the non-planar illumination architecture, sensitivity, and experimental results of arbitrary apex angle axicons.

© 2022 Optica Publishing Group

<https://doi.org/10.1364/OL.465046>

Introduction. Axicons are rotationally symmetric, convex prisms commonly used in optical alignment, Bessel-beam generation, and atom-trapping [1]. Common features of interest include overall apex angle, cone tip geometry, and azimuthal profile linearity. However, because of their steep and convex geometry, they are difficult to measure with non-contact techniques [2,3]. Axicons are measurable on a coordinate measuring machine (CMM), but sampling is pointwise and limited. Interferometry is reliable and fast, but requires a null optic for a given apex angle. Measuring with confocal microscopy or white light interferometry requires no null; yet, the slopes of a cone necessitate stitching between many clocked sub-apertures to construct a full aperture map.

Deflectometry, a non-null metrology technique, has been shown to provide surface accuracy similar to interferometry [4]. Typical setups use a spatially well-defined, planar source such as a pixelated liquid crystal display (LCD) to illuminate the unit under test (UUT). By using a camera to observe the light reflected at the UUT from the source, the corresponding points at the camera, UUT, and light source are determined. These correspondences are used to calculate slopes at each UUT point, which then integrate into surface height. Usually, the range of measurable surface slopes is limited by the planar source's size.

In some cases, an auxiliary optic such as a high-quality cone allows a planar source to be remapped and measure extremely sloped surfaces with deflectometry [5]. Curved LCD screens extend the slope-measurement range, but are calibration intensive [6]. A clocking deflectometer offers a hemispherical 2π steradian measurement range, but trade-offs with longer acquisition times and sub-aperture stitching must be carefully considered [7].

Non-planar illumination configuration. *Cylindrical scanning architecture.* As an alternate strategy to using planar array sources, we propose a cylindrical illumination architecture for measurement. Its schematic non-planar geometry is illustrated in Fig. 1.

The test geometry coaxially aligns a camera, optic, and surrounding illumination source. In the literature, Diaz-Urbe and Moreno-Oliviera made significant contributions toward the test of convex aspheres with this coaxial layout by using a cylindrical paper screen with printed fiducials [8,9]. Similarly, Campos-Garcia devised a scanning method that clocks two linear arrays of sources about a convex sphere [10]. In this family of techniques, the spacing of fiducials/mask holes along a meridian was designed to obtain uniform radial spacing in the images of the UUT for improved integration of centroided spot locations.

Our setup adopts identical first-order geometry, but implements custom scanning sources to obtain dense surface slope measurements. Two non-planar sources, of different shapes, move in different trajectories to trace the same cylindrical surface enclosing the UUT. First, an annular source with fixed radius ρ moves in \hat{z} , “descending” through the optic. Then, a vertical line source revolves $\phi = 2\pi$ at radius ρ about the cylinder axis.

By recording the reflected signal into the camera at each scan step, we may disambiguate the source locations \bar{z}_c and $\bar{\phi}_c$ that observe maximum irradiance and satisfy the law of specular reflection across each UUT point, r_{uut} . The ring source sweeps the vertical step positions z_i for $i \in [1, M]$, while the line source sweeps the azimuthal step positions ϕ_j for $j \in [1, N]$, and M and N are the final indices of the source positions that illuminate that pixel. Here, I_i and I_j are a recorded pixel's irradiance at each scan position. A first-moment centroid is used to discover which \bar{z}_c and $\bar{\phi}_c$ provoke the strongest response at each pixel of

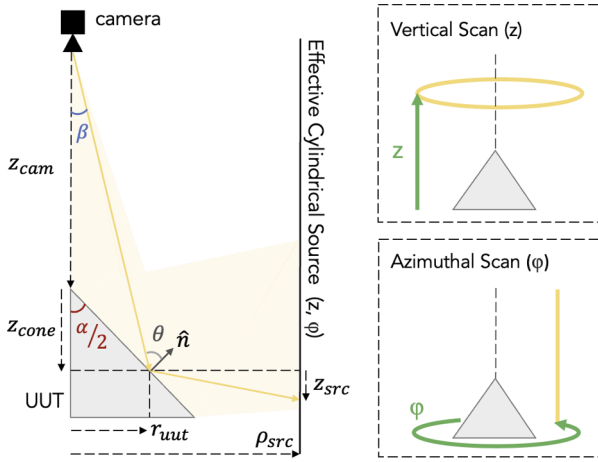


Fig. 1. Section view, where each UUT point, $r_{uut}(x, y, z)$, maps to a cylindrical source location, $r_{src}(\rho, \phi, z)$. The conical apex angle is α , camera view angle is β , camera-to-apex distance is z_{cam} , and source radius is ρ_{src} . Drawn in reverse, a representative ray (yellow) reflects at θ relative to the surface normal \hat{n} . Two scans of the independent sources (yellow) move in \hat{z} and $\hat{\phi}$ (green) to implement the non-planar illumination source.

the UUT.

$$\bar{z}_c = \frac{\sum_{i=1}^M z_i I_i}{\sum_{i=1}^M I_i}, \quad \bar{\phi}_c = \frac{\sum_{j=1}^N \phi_j I_j}{\sum_{j=1}^N I_j}. \quad (1)$$

With the corresponding illumination source coordinates to each UUT pixel discovered, we convert back to Cartesian coordinates $\vec{r}_{src}(\rho, \phi_c, z_c) = \vec{r}_{src}(x, y, z)$, and proceed with slope calculations as usual per the usual deflectometry method [4].

This non-planar illumination deflectometry (NPID) scheme is also applicable for testing convex aspheres, but measurement of surfaces with a continuous vertex will have a large obscuration due to requiring an infinitely tall cylinder and distant camera at z_{cone} to illuminate the aperture center. Radiometric issues also arise because of these surface points at the vertex view distant regions of the illuminating cylinder. Here, the subtended solid angle is extremely oblique and much less radiance is transferred to the detector pixels. For axicons measured with a large z_{cam} , an elegant radiometric consequence is that the UUT's nominally constant slopes along each azimuth cause the full conical aperture to obtain nearly uniform illumination from the cylinder.

Cylindrical source height and slope sensitivity. Referring to Fig. 1, the equation of the modeled cone is $z_{sag} = -\cot(\alpha/2)\sqrt{(x-x_0)^2 + (y-y_0)^2} + z_0$, centered at (x_0, y_0, z_0) . Analytically, the source position, z_{src} , that corresponds to the slope at a radial position of the test axicon, r_{uut} , is given as

$$z_{src}(r_{src}) = \frac{r_{src} - r_{uut}}{\cot(\theta - \alpha/2)} = \frac{r_{src} - r_{uut}}{\tan(\alpha - \beta)}. \quad (2)$$

We can derive the sensitivity to slope change with respect to the angle of incidence relative to the surface normal:

$$\frac{dz_{src}(r_{src})}{d\theta} = \frac{r_{src} - r_{uut}}{\cos^2(\theta - \alpha/2)}. \quad (3)$$

After the derivative is taken, we recognize that the surface slope changes at twice the rate of the angle of incidence, $dS \approx d\hat{n} = d\theta/2$. The law of error propagation states the influence of the illumination linewidth, number of samples, and signal-to-noise ratio, $\sigma_{src\ change} = w_{line}/(N_{steps}^{1/2} \cdot \text{snr})$ [7]. The linewidth

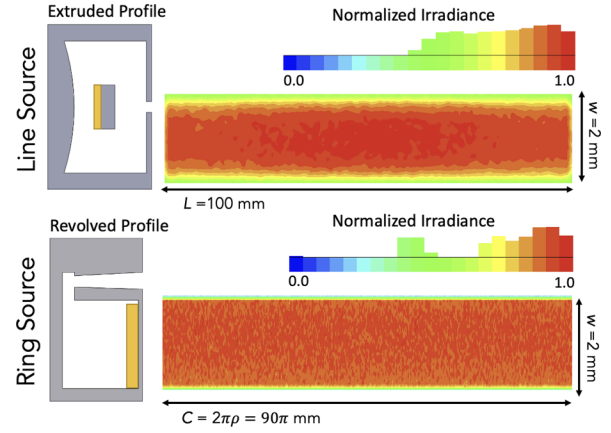


Fig. 2. Both sources are modeled in SolidWorks and LightTools. Walls are modeled with a \cos^5 scattering distribution and 2% loss per reflection. 20 million rays are traced and sampled for both $\sim 401 \times 41$ cylindrical and linear detectors, achieving a $>40^\circ$ and $>30^\circ$ half-angle intensity, respectively. Decreasing cavity surface area increases source radiance at the cost of spatial integration. Both simulations possess less than 15% average deviation across their irradiance meshes.

is defined as physical width of the reflected light source at the axicon surface, viewed from the camera. Together,

$$dS = \frac{\sigma_{src\ change} \cdot \cos^2(\theta - \alpha/2)}{2(r_{src} - r_{uut})}. \quad (4)$$

This relationship guides the design of the test configuration scale. Smaller linewidth and step size increase the slope sensitivity at the cost of measurement time and motion control resources.

Illumination cavity design. Figure 2 shows the line and ring illumination designs, both inspired by integrating sphere scattering [11]. Power radiates from numerous small, uniformly spaced pseudo-Lambertian sources (shown in yellow) inside a cavity. By ray recirculation, rays scatter between the non-specular interior walls until the rays' position and angle fit within the spatio-angular envelope required to escape the cavity geometry [12]. Uniform, Lambertian distributions emerge from the 2-mm-wide exit slits.

Once illumination designs were satisfactory, solid models were split into multiple components for 3D printing and assembly. White 3D-printed plastic provided the interior chamber components, while black plastic baffled stray light. Surfaces were roughened to increase scattering. The light source within both cavities was an LED strip (Model #CB-62K, 24 V, FlexFire LEDs). Figure 3 shows each source in its scanning configuration and its corresponding views of the UUT from the camera.

Experimental setup and system alignment. Figure 4 shows all of the involved system hardware. A Point Grey monochromatic camera (FL3-U3-13Y3M-C) with an $f = 25$ -mm lens (Computar M2514-MP2) views the axicon UUT. A 3-mm pinhole was 3D printed and placed at the front of the lens. The two uncoated fused silica axicons, with nominal apex angles $\alpha = 100 \pm 0.02^\circ$ and $\alpha = 140 \pm 0.02^\circ$ (manufacturer's specification) were mounted and measured in an testing identical setup, differing only by the descending ring's initial height. The positions of the camera pinhole, axicon mount base, and both illumination sources were calibrated by a CMM and digital

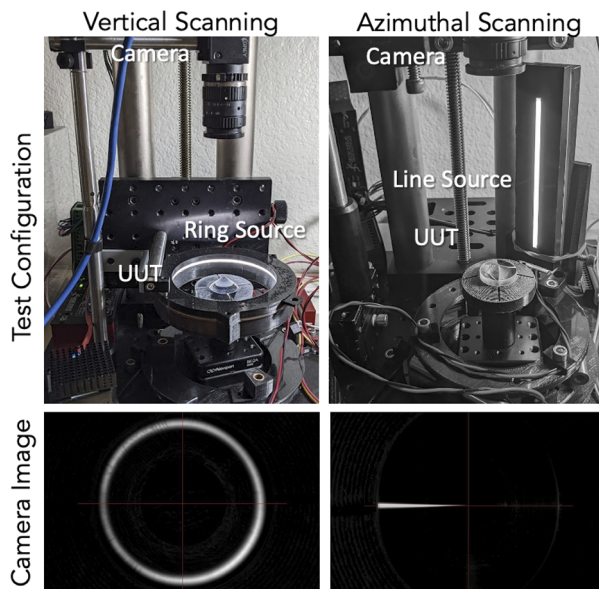


Fig. 3. The vertically scanned ring source illuminates an annulus of the ϕ 25.4-mm, 100° axicon. Conversely, the azimuthally scanned *line source* illuminates a pseudo-triangular slice of a ϕ 25.4-mm, 140° axicon. Over either full scan range, all points across the full apertures are illuminated except the central ϕ 455- μ m region. Axicon manufacturing naturally rounds the conical tip, so the centermost 15 pixels are out of the dynamic measuring range of this NPID system.

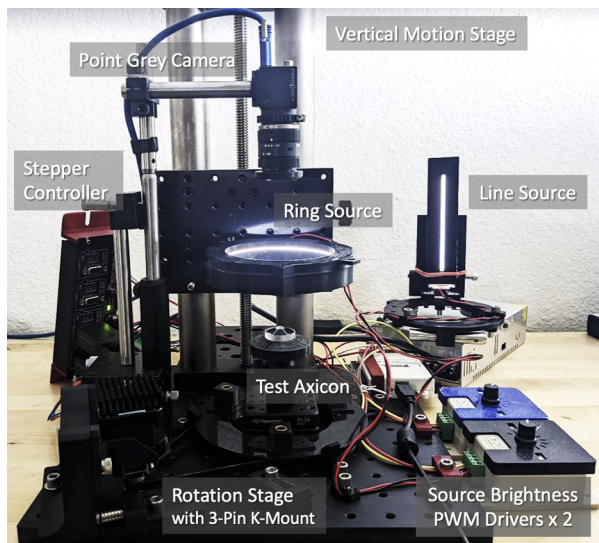


Fig. 4. Camera and ring source both have four degrees of freedom (DOFs) in XY decenter and tip/tilt for coaxial alignment, while the line source platform could only be moved in XY decenter. A flat reference mirror and a camera digital crosshair are key tools for alignment. Notably, excess tip/tilt between the ring source and the axicon result in a cardioid-shaped signal rather than the nominal halo seen in Fig. 3.

calipers, accurate to 5 μ m and 10 μ m, respectively. This placed the hardware in the same coordinate system used for slope calculation.

The ring source was mounted on a vertical lead screw stage, with a measured 5.81 μ m root mean square (rms) position repeatability. The line source was mounted to a custom belt-driven rotation stage with 0.02° rms position repeatability. A quasi-kinematic 3-pin mount was designed into the rotation stage platform. This feature allowed for the line source to be inserted and removed after azimuthal scanning, so vertical scanning could subsequently be performed. During a given scan of one source, the other must be relocated to avoid interference.

For motion control, Matlab communicated with a National Instruments DAQ (Model USB-6008) to send commands to a GeckoDrive G540 stepper motor driver. Brightness at each source was controlled by an independent pulse width modulation circuit.

Toward camera alignment with the axicon, we first aligned the camera's axis normal to the optical breadboard (our set plane reference). A reference flat mirror was placed at the breadboard base and the camera was tip/tilted until its aperture image was centered in the vision software's central digital crosshair. Then, after replacing the mirror with the mounted UUT, we focused the camera at the axicon tip and decentered the UUT until the tip met the crosshair center. Finally, the camera was focused at the axicon's base, and image processing verified that the image of this circular edge was elliptical only up to one pixel.

For light source alignment, annular 3D-printed cylindrical alignment aids and steel cylindrical pins coarsely mated the camera lens barrel, ring source, and annular line source rotation stage. We then verified the fitted axis locations of the hardware on the CMM and calipers up to the uncertainty of the CMM; however, remaining decenters and tilts between hardware components must be considered.

Alignment sensitivity was analyzed by simulating the NPID system in Zemax and Matlab. Simulated misalignments, such as 10- μ m decenter and 1-mrad tip/tilt and for either axicon and either source, contributed <100 -nm rms of shape error, mostly in defocus, spherical, and coma. The steeper 100° axicon was more sensitive to misalignment errors in the Z-direction, showing up 266 nm of error in defocus when the axicon or ring source height was miscalibrated by 10 μ m.

Measurement results. Acquisition and centroiding. The 100° axicon was vertically scanned in 25- μ m steps over 10 minutes and about a full revolution in 0.225° steps in 20 minutes. Using the same step increments, the 140° axicon was vertically scanned in 17 minutes and azimuthally in 20 minutes. Since discrete motions take a minimum of 0.5 s, and limited hardware was available to the authors, the total acquisition time is dominated by the motion hardware rather than the fundamentally required exposure. For a larger budget, the system speed will be substantially improved.

The scan signals for one pixel of the measured 100° axicon is shown in the first row of Fig. 5. Calculating the centroids, one \hat{z} and $\hat{\phi}$ are assigned to each pixel of the $\sim 843 \times 843$ aperture maps. Figure 5 shows these centroid maps for the same optic in the second row. Noise was rounded up to one count, yielding $\text{snr}_{100^\circ} \approx 175$ and $\text{snr}_{140^\circ} \approx 167$. Using the sensitivity relationship [Eq. (4)] with the nominal incidence angle θ reflected at each axicon's half-radius, we arrive at $dS_{\text{NPID}, 100^\circ} = 18.22 \mu\text{rad}$ rad and $dS_{\text{NPID}, 140^\circ} = 7.65 \mu\text{rad}$.

Reconstruction results. Using both centroid maps from each full test and assuming nominal cone geometry for triangulation calculations, surface slopes were processed and height measurements were obtained by Southwell integration. Both 100° and

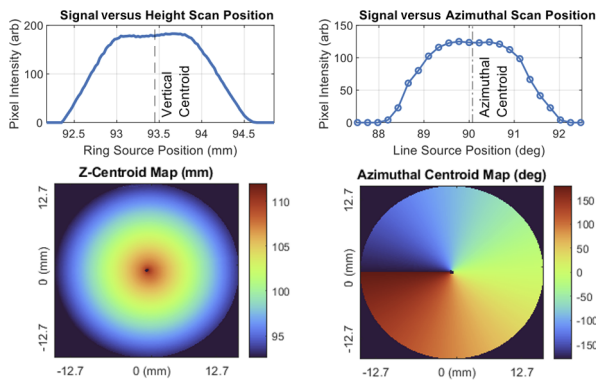


Fig. 5. At one half radius from the 100° UUT’s center, a representative pixel observes 91 signal points in the height scan and 18 points from the azimuthal. At an analogous position, a representative 140° UUT pixel observes 122 and 18 points, respectively. Height and azimuthal centroid maps indicate the source locations of greatest specular response.

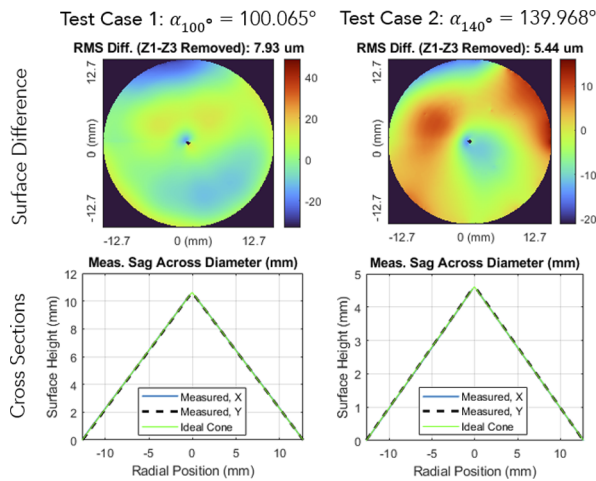


Fig. 6. By removing piston, tip, and tilt, the best-fit cone angles and diametrical profiles for (α_{100° , α_{140°) of the NPID measurements show consistency with the CMM measurements and also profile linearity in cross sectional slices.

140° test scenarios were processed with identical calibration parameters (i.e., geometrical positions of the hardware), differing only in height scan start position and scan range (17 mm and 25 mm, respectively). The difference maps between NPID reconstructions and their respective best-fit cones are shown in Fig. 6. There is remarkable similarity in the apex angle measured by the TESA micro-hite 3D CMM, which were 100.06° and 139.93° when sampled and fitted from 300 points each. Qualitatively inspecting the difference maps, we discern visible mid-high spatial frequency content, which often pervades mass-produced industrial optics.

Subtracting Zernike terms up to Z_{22} and Z_{37} from the difference maps, we note that the rms difference converges toward below 1 μm , i.e., $\sigma_{rms, 100^\circ, Z22} = 1.74 \mu\text{m}$ and $\sigma_{rms, 100^\circ, Z37} = 1.44 \mu\text{m}$, while $\sigma_{rms, 140^\circ, Z22} = 0.98 \mu\text{m}$ and $\sigma_{rms, 140^\circ, Z37} = 0.60 \mu\text{m}$. While the convergence of these rms quantities toward sub-

micron values aligns with the expected nature of optically polished surfaces, further system calibration with a high-quality axicon or a random/rotation averaging test will remove the remaining systematic shape error. This calibration step will allow the absolute mid-high spatial frequency information to be obtained. Just like for other deflectometers, the quality of calibration and alignment strongly influences the measurement result.

Conclusion. We present an illumination strategy that efficiently probes convex conical surfaces. The configuration has distinct trade-offs from typical planar-illuminated, phase-measuring deflectometry setups [4]. Despite advantages of speed and accessibility, planar screens require vast areas or must be strongly tilted to accommodate steep test optics and will still struggle with radiometric uniformity due to oblique radiance transfer geometry [12].

By measuring convex optics with NPID, we relinquish the benefits of planar deflectometry in favor of desirable radiometry and compactness, and obtain freedom from sub-aperture stitching and null references. Since designing, building, and precisely moving custom sources is a realizable task, applying NPID can be very versatile. For example, building the same system in the infrared allows rough convex optic measurement, or modifying the source designs for even higher radiance allows measurement of dark, specular objects. Specifically, an upscaled NPID will be highly useful to measure large obscured convex mirrors, which are the secondary element in Ritchey–Chrétien Cassegrain telescopes, and also gives, which are a narrow nose cone shape commonly used in aerodynamics. The method serves to broaden the dynamic slope-measuring range and the metrology community’s toolbox of accessible cross-checking techniques.

Disclosures. The authors declare no conflicts of interest.

Data availability. Data underlying the results presented in this paper may be obtained from the authors upon reasonable request.

REFERENCES

1. J. H. McLeod, *J. Opt. Soc. Am.* **50**, 166 (1960).
2. H. Gao, X. Zhang, and F. Fang, *Meas. Sci. Technol.* **28**, 095204 (2017).
3. Z. Wei, Q. Yuan, X. Ma, J. Hu, A. Zeng, and H. Huang, *Opt. Commun.* **434**, 23 (2019).
4. J. Burke, A. Pak, S. Höfer, M. Ziebarth, M. Roschani, and J. Beyerer, “Deflectometry for specular surfaces: an overview,” arXiv:2204.11592 (2022).
5. M. J. F. Carvalho, C. L. N. Veiga, and A. Albertazzi, *J. Braz. Soc. Mech. Sci. Eng.* **41**, 380 (2019).
6. C. Liu, Z. Zhang, N. Gao, and Z. Meng, *Opt. Express* **29**, 43327 (2021).
7. L. R. Graves, H. Quach, H. Choi, and D. W. Kim, *Opt. Express* **27**, 7602 (2019).
8. R. Díaz-Uribe and M. Campos-García, *Appl. Opt.* **39**, 2670 (2000).
9. V. I. Moreno-Oliva, M. Campos-García, and R. Díaz-Uribe, *J. Opt. A: Pure Appl. Opt.* **10**, 1040209 (2008).
10. M. Campos-García, R. Díaz-Uribe, and F. Granados-Agustín, *Appl. Opt.* **43**, 6255 (2004).
11. R. J. Koshel, *Illumination Engineering: Design with Nonimaging Optics*, 1st ed (Wiley, 2013), .
12. H. Quach, H. Kang, H. Choi, and D. W. Kim, *Proc. SPIE* **11487**, 114870L (2020).